Lithium storage behaviour of AgNbO3 perovskite: Understanding electrochemical activation and charge storage mechanisms

Abbas Khan, Metin Orbay, Nicolas Dupré, Eric Gautron, Etienne Le Calvez, Olivier Crosnier, Andrea Balducci, Thierry Brousse

Lithium storage behaviour of $AgNbO_3$ perovskite: Understanding electrochemical activation and charge storage mechanisms

Abbas Khan[a,b], Metin Orbay[c], Nicolas Dupré[a], Eric Gautron[a], Etienne Le Calvez[a,b], Olivier Crosnier[a,b], Andrea Balducci[c], Thierry Brousse[a,b]

[a] Nantes Université, CNRS, Institut des Matériaux de Nantes Jean Rouxel, IMN, F-44000 Nantes, France
[b] Réseau sur le Stockage Electrochimique de l'Energie (RS2E), CNRS FR 3459, 80039 Amiens, France
[c] Friedrich-Schiller-University Jena, Institute of Technical Chemistry and Environmental, Chemistry and Center for Energy and Environmental Chemistry, Jena, Germany

Abstract

In this study, a model $AgNbO_3$ perovskite is prepared via polyacrylamide synthesis technique, and the underlying unique Li^+ storage mechanism is studied. This structure is projected to provide low Li^+ storage capacity due to all occupied crystallographic sites. It delivered a specific capacity of 17 $mAh.g^{-1}$ at 0.1$A.g^{-1}$ within the potential range of 1.2-3.0V *vs.* Li^+/Li. However, at lower potentials, the material undergoes activation for Li^+ storage by a multistep structural transition that included in-situ Ag-exsolution from the A-site of the lattice and an electrochemically induced crystalline-to-amorphous transition. At low potential the materials delivers high specific capacity (226 $mAh.g^{-1}$ at 0.1 $A.g^{-1}$ in 0.01-3V *vs.* Li^+/Li potential range) due to the contribution of improved Nb-redox activity and nanoscale Ag-Li (de)alloying mechanisms that were comprehensively examined utilizing advanced characterization tools. In addition, good capacity retention of 72 $mAh.g^{-1}$ at high current density of 2$A.g^{-1}$ and an excellent cyclic stability with coulombic efficiencies above 99.9% are obtained for 2500 cycles at 1 $A.g^{-1}$ underlining the performance and the stability of $AgNbO_3$. This study introduces an alternative approach for tailoring electrode material using an electrochemically driven in-situ activation process. It also serves as a paradigm for the use of exsolved materials as negative electrodes in fast-charging batteries, paving the way for a better understanding of charge storage mechanisms in perovskites.

1. Introduction

With the successful commercialization of electric vehicles, the demand for energy storage devices is becoming increasingly critical [1]. Lithium-ion batteries (LIBs) are nowadays used in many applications, including several high-power applications. In these LIBs graphite is used as negative electrode material, and it is important to notice that despite the favorable feature of this type of anode, its use might not be an optimal choice when high current densities are applied [2]. As a matter of fact, the power performance of this material is rather different for the charge (intercalation) and the discharge (de-intercalation) process. It has been shown that during the discharge process graphite anodes retain well their capacity, but their performance during the charge process is strongly affected by the applied current [3]. Clearly, this represents a limitation associated to the use of this carbon electrode.

In the past years several alternative materials have been explored in literature. Among them, lithium titanium oxide ($Li_4Ti_5O_{12}$) has been one of the most widely investigated, and this anodic

material is used as high-power alternative to graphite in commercial devices utilized for niche applications such as short-range buses but suffers from low energy density due to overall lower cell voltage [4]. Among other alternatives, niobium (Nb) containing oxides such as Nb_2O_5 and binary oxides L-Nb-O (where L is Ti, Fe, Zr, etc.), have gained an increasing attention in the last years. Anodes based on these materials display high specific capacity, originating from rich redox activity (Nb^{5+} to Nb^{4+}, Nb^{4+} to Nb^{3+}), fast charging capability, safety and excellent cyclic stability [5–8].

ABO_3 type perovskites such as $AgNbO_3$ are versatile materials because of their capacity to tolerate wide range of cation sizes, oxidation states, dopants and defects [9]. In this structure, A-site is filled by large radii cation in the center of perovskite cage with 12-fold coordination, and corner-shared BO_6 octahedral network giving a high packing factor [10]. The exploration of high voltage perovskite anodes [11] and exsolved perovskites for energy storage applications has shown promising results, yet the latter faces rapid capacity decline with cycling [12]. The challenge in utilizing ABO_3 type perovskites to their full potential lies in the difficulty of incorporating Li^+ ions into their structure due to limited interstitial sites and the constraint of fixed lattice spacing. Overcoming this obstacle is crucial for maximizing the energy storage capabilities of these materials.

One potential strategy to activate such materials is to partially substitute the A-site of the structure with cations at higher oxidation state to induce vacancies. Recently, it has been shown that this strategy can be successfully implemented through the substitution of Ag^+ cations by La^{3+}, leading to the creation of A-site vacancies in $Ag_{1-3x}La_x\square_{2x}NbO_3$ (with $x \leq 0.20$ and where $\square$ is a A-site vacancy) [13]. Moreover, the corresponding substituted materials have demonstrated fast Li^+ insertion and a dependence of the capacity with the number of created vacancies to a certain extent. Although the capacity of these materials is lower than that of other niobates such as T-Nb_2O_5, $CeNb_3O_9$, $Ti_2Nb_2O_9$, $TiNb_2O_7$, or $HTiNbO_5$ [14–18] the power capability of this compound made it of interest for further investigations.

An alternative appealing strategy which could be utilized to further improve the specific capacity of this type of material is the promotion of *in-situ* activation. Recently, it has been reported that *in-situ* amorphization can be an efficient way to generate defects by breaking the long-term crystal orders, hence enriching the Li^+ insertion sites to obtain enhanced specific capacity [19,20]. However, transitions from crystalline materials to amorphous ones are challenging to realize, especially in ABO_3 type perovskites (with ideal 1:1 cation ratio), due to strong structural stability and has rarely been achieved. It is also interesting to observe that ABO_3 type perovskites have received significant attention for realizing exsolution processes, a strategy to grow metallic nanoparticles from its host structure [21–24], especially for solid oxide fuel cells. The occurrence of this type of process could also be of interest in view of the use of ABO_3 type perovskites in LIBs.

In this study we report a detailed structural and electrochemical investigation on the storage mechanism occurring in a model ABO_3 type perovskite, namely $AgNbO_3$. The aim of this work is to evaluate whether it is possible to electrochemically promote, and possibly control, the occurrence of *in-situ* activation and exsolution processes in order to improve the capacity of $AgNbO_3$ based electrode as well as their behavior under high current density.

2. Experimental section

Material synthesis

$AgNbO_3$ perovskites were synthesized by polymerization assisted sol-gel route named polyacrylamide synthesis, which has been adopted previously for synthesis of transition metal oxides [25]. Stoichiometric amounts of silver nitrate ($AgNO_3$ by Alfa Aesar, 99.9%) and niobium oxalate hydrate ($C_{10}H_5NbO_{20}$. xH_2O by Alfa Aesar) precursors were dissolved in ethylene glycol (Alfa Aesar) and stirred at room temperature. Citric acid ($HOC(CH_2CO_2H)_2$ by Alfa Aesar, 99+%) was added to the solution in 1.5:1 cation molar ratio and stirred until transparent solution was obtained. Citric acid acted as a complexing agent of which carboxyl and hydroxyl groups were attached to Ag^+ and Nb^{5+}, respectively, through chelation reaction. Afterwards, acrylamide monomers (Alfa Aser) and N, N′-mesthylene-bisacrylamide (Alfa Aser) cross linkers were introduced to the solution in 9:1 cation molar ratio. The monomer radicals open up the double bonds of acrylamide and form a new activation site, which provides linkage to the second monomer unit and thus propagates the chain process by radical transfer process. Polyacrylamide grows in a linearly chained system. However, N, N' –methylene bisacrylamide acts as cross-linker and help to grow and develop a 3D network of interconnected loops. The solution was heated to 90 °C while stirring and hydrogen peroxide (30% w/w H_2O_2 in H_2O by Sigma Aldrich) was added to initiate the polymerization. Polymeric gel is formed after 20 min and converted to xerogel when kept in oven at 300 °C. The final $AgNbO_3$ materials were obtained by grounding xerogel and annealing at 650 °C in air for 12 hrs. The synthesis process is schematically illustrated in Fig. 1a.

Physical characterizations

Powder XRD measurements were carried out using PANalytical X'Pert Pro-diffractometer (Malvern PANalytical, Almelo, Netherlands). Cu-$K_{\alpha1}$-$K_{\alpha2}$ (λ = 1.54060 Å, 1.54443 Å) radiation source with acceleration voltage of 40 KV at a current 40 mA was used. XRD data were recorded in the 2θ range of 5° to 80°, scanning at a step size of 0.0170°. For *in-situ* XRD measurements, a specially designed Swagelok-type® cell with beryllium window on top was used [26]. The data were collected at different 2θ ranges between 20° and 80°. The applied current density, pattern acquisition and relaxation time varied depending on the selection of potential window for GCPL measurements. The BET specific surface area of the $AgNbO_3$ powder was calculated using N_2 adsorption–desorption isotherms at 77K with a Quantachrome Nova 4200e equipment (Anton Paar). The morphology study of $AgNbO_3$ powders and *post-mortem* analyses of cycled electrodes were performed by Zeiss MERLIN Instrument using in-Lens annular detector keeping an operating voltage of 20 kV. To prepare the samples, a small fraction of powder/electrode were affixed on carbon double tape. *Ex-situ* ^{7}Li and ^{93}Nb MAS NMR experiments were acquired on a Bruker Avance 500 spectrometer (B_0=11.75T), Larmor frequencies ν_0 (^{93}Nb = 122.41 MHz, ^{7}Li = 194.37 MHz) at RT. A Bruker MAS probe with a cylindrical 2.5 mm (o.d) zirconia rotor spun at a frequency of 25 kHz was used for spectral

analyses. Spectra were obtained by applying a single pulse sequence, and a recycle delay (D_1) of 3 seconds ensuring the acquisition of quantitative spectra. The resulting integrated intensities were normalized with respect to the mass of the sample contained in the NMR rotor, the number of scans, and the receiver gain. Scanning/transmission electron microscopy (S/TEM) measurements were performed to characterize the morphological modification and Nb oxidation states of the pristine sample and after cycling (0.01V *vs.* Li+/Li). For both samples, the powder has been brought into contact with a holey carbon film-coated copper grid in a glove box (Ar atmosphere). The grid was inserted in an aberration-corrected S/TEM Themis Z G3 (Thermo Fisher Scientific) using an atmosphere-controlled sample holder. All S/TEM experiments were performed at 300 kV.
High-angle annular dark-field (HAADF-STEM) images were acquired with 21.4 mrad convergence angle and 63–200 mrad collection angles. A Super-X system (four energy-dispersive X-ray detectors) allowed to acquire elemental maps.
Electron energy loss spectroscopy (EELS) was performed with a GIF Quantum ERS 966 imaging filter (Gatan) in Dual-EELS mode (for simultaneous acquisition of low loss and high loss spectra) in STEM mode (21.4 mrad convergence angle and 36 mrad collection angle, probe current ~50 pA). The spectra presented here were integrated on spectral image areas. A power law was used to subtract the background before core edges.

Electrochemical measurements

Slurries containing 85% wt. active material ($AgNbO_3$), 10% wt. conducting agent (Imerys Super C65) and 5% wt. binder (Walocel sodium carboxymethyl cellulose CMC2000) were prepared and cast onto either copper or aluminum foil *via* doctor blading. $AgNbO_3$ electrode mass loadings ranged from 1.2 to 2.5 $mg.cm^{-2}$. For *in-situ* XRD, free standing electrodes were prepared by mixing $AgNbO_3$, conductive agent (Carbon Black by Superior Graphite, Chicago, IL, USA) and poly (1,1,2,2-tetrafluoroethylene (PTFE, Sigma Aldrich) in a %wt. of 75, 15, and 10, respectively. Few drops of ethanol were added, and the mixture was grounded until get homogenous paste. The paste was processed via cold-rolling until it became an electrode of around 5–10 $mg.cm^{-2}$. The latter formulation, different from the one used for electrochemical tests, was chosen to ensure high quality in-situ XRD measurements. Propylene Carbonate (PC) anhydrous 99.7 % was purchased from Sigma Aldrich. Lithium bis(trifluoromethanesulfonyl)imide (LITFSI) (99.9 %), lithium bis(fluorosulfonyl)imide (LIFSI) (99.9 %) and 1-Butyl-1-methylpyrrolidinium bis (trifluoromethanesulfonyl)imide ($Pyr_{1,4}TFSI$) were purchased from Solvionic and used to prepare the electrolytes at room temperature whereas LP30 (Solvionic) was used as is. Swagelok-type® cells were used to study the electrochemical performance of $AgNbO_3$ electrodes in a three-electrode cell setup. The working electrode (WE) was $AgNbO_3$, whereas the reference electrode (Ref) and the counter electrode (CE) was lithium metal. Biologic VMP-3 and MPG-200 potentiostats were used for all electrochemical studies. The total area of all electrodes was 1.13 cm^2. Diffusion coefficient of $AgNbO_3$ electrodes were measured using the galvanostatic intermittent titration technique (GITT), using a previously described protocol [27]. Cell assembly and electrolyte preparation were carried out in an argon-filled glovebox (O_2 and H_2O <1 ppm).

3. Results and Discussions

Crystal structure and characterizations of $AgNbO_3$

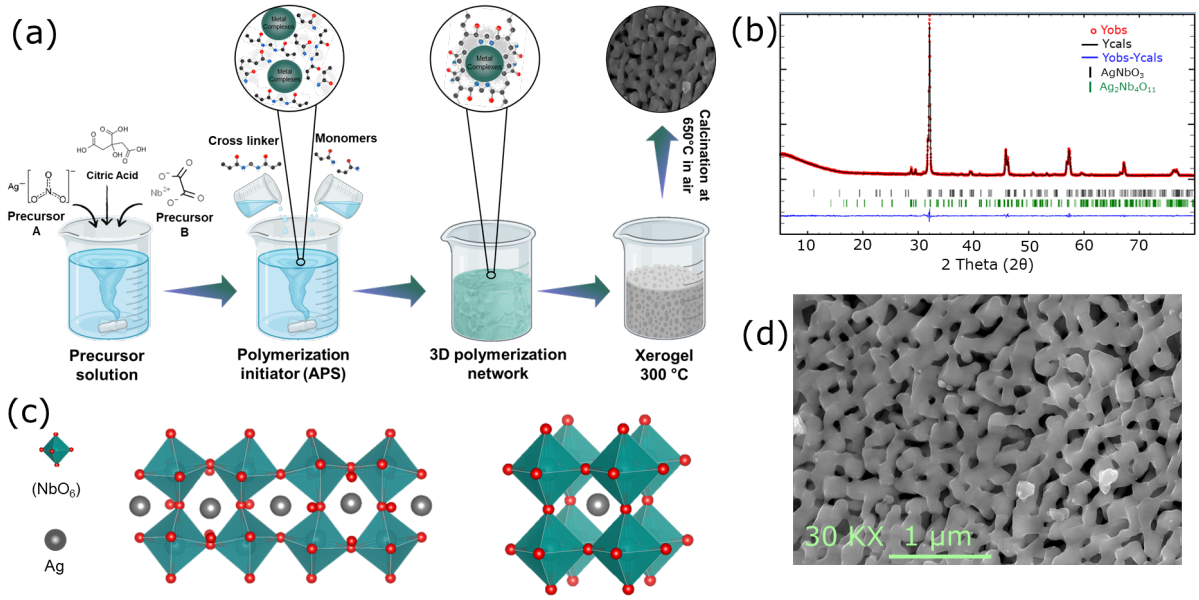

Figure 1. (a) Schematic illustration of polyacrylamide synthesis of $AgNbO_3$ perovskites. (b) Rietveld refined XRD profile of $AgNbO_3$ powder with experimental and calculated patterns, as well as the difference between the two patterns. Bragg reflection of the $AgNbO_3$ perovskite phase is denoted by black bars. $AgNbO_3$ crystalized in an orthorhombic perovskite phase (Pbcm space group with cell parameters a = 5.5485(16) Å, b = 5.6001(14) Å, and c = 15.6475(4) Å). Few impurities (mass percentage of ~11%) with main diffraction peaks around 29° corresponds to $Ag_2Nb_4O_{11}$ phase denoted by green bars. (c) Top and 3D view of crystal structure of $AgNbO_3$ based on refinement results. (d) SEM image of material showing well-defined and uniform morphology of $AgNbO_3$.

An overview of the synthesis of $AgNbO_3$ is presented in Fig.1a. Rietveld refinement of powder X-ray diffraction pattern revealed the formation of orthorhombic perovskite phase (Pbcm space group) with lattice parameters a = 5.54857(16) Å, b = 5.60010(14) Å, and c = 15.6475(4) Å (Fig. 1b). The cell parameters indicate a clear difference between the a and b parameters, validating the use of orthorhombic space group [28]. The perovskite structure of $AgNbO_3$ is built by Ag^+ cations in the center of the perovskite cage with a coordination number of 12 while Nb^{5+} with coordination number of 6 form corner-shared tilted [NbO_6] octahedra as shown in Fig. 1c. The average crystallite size obtained is 76.8 nm, calculated by using Scherrer equation. The detailed Rietveld refinement results are presented in supplementary information (Table S1). Small impurity peaks (diffraction peak at 29°) of $Ag_2Nb_4O_{11}$ can be found in $AgNbO_3$ X-Ray diffraction pattern of the corresponding powder. The main reason of this is the thermodynamic instability of Ag^+ at higher temperatures (conversion to Ag^0 at 150°C), which is causing a phase formation competition between $AgNbO_3$ and $Ag_2Nb_4O_{11}$ [28,29]. Taking these results into account, it is evident that the realization of a single phased $AgNbO_3$ with

uniform morphology via conventional solid-state reaction routes is rather challenging. Approaches such as keeping slight excess of Ag_2O precursor during synthesis or sintering in high-pressure O_2 environment has been reported to favor the homogeneity and improved phase quality of $AgNbO_3$ [29]. We recently reported the synthesis of $Ag_{1-3x}La_x\square_{2x}NbO_3$ (with $0 \leq x \leq 0.20$) perovskites by sol-gel method with fewer impurities [13]. However, to avoid particle agglomeration and to obtain a uniform morphology, polyacrylamide synthesis route was adopted for $AgNbO_3$ material [30]. The polymerization step during synthesis process helps to bind the metal complexes in solution with even distribution leading to the formation of interconnected porous network of particles with a uniform morphology, as shown in Fig. 1d. The BET surface area of the $AgNbO_3$ synthesized by polyacrylamide route was 6.7 m^2g^{-1}, which represents a twofold increase compared to materials synthesized by sol-gel method [13]. The electrochemical behavior of composite electrodes containing the synthesized $AgNbO_3$ was initially investigated in half-cell configuration (the details are reported in the experimental part). Preliminary measurements were performed in the potential range between 1.2 – 3.0V *vs.* Li^+/Li, which the electrochemical window mostly used to investigate electrodes containing Nb-based oxides [31]. Due to the 100% occupancy of the A site by Ag^+ cations in the $AgNbO_3$ structure, there are no open channels in the structure for Li^+ diffusion, nor well-defined empty sites to welcome them. Hence, no significant redox activity is observed in the CV within such potential window and the electrode displays a very limited specific capacity of 17 $mAh.g^{-1}$(Fig. 2a). This capacity mostly originated from surface charge storage processes rather than insertion of Li^+ into the structure. To confirm any structural changes in the material upon cycling, *in-situ* XRD experiments were carried out. The crystallographic peaks of perovskite structure do not deviate from their original positions, and no additional peaks appear upon charge/discharge processes, as shown in Fig. 2b. These results indicate that in the investigated potential range (1.2 – 3.0V *vs.* Li^+/Li) the electrode is displaying a stable structure containing Ag^+ and Nb^{5+}. It is interesting to notice, however, that a prolonged cycling process is leading to the formation of few nanoparticles on the surface (probably Ag^+ to Ag^0 conversion), although the morphology is retained. This latter point is well visible from the differences of the surface on *ex-situ* SEM observations reported in Fig. 2c and in Fig. 2d.

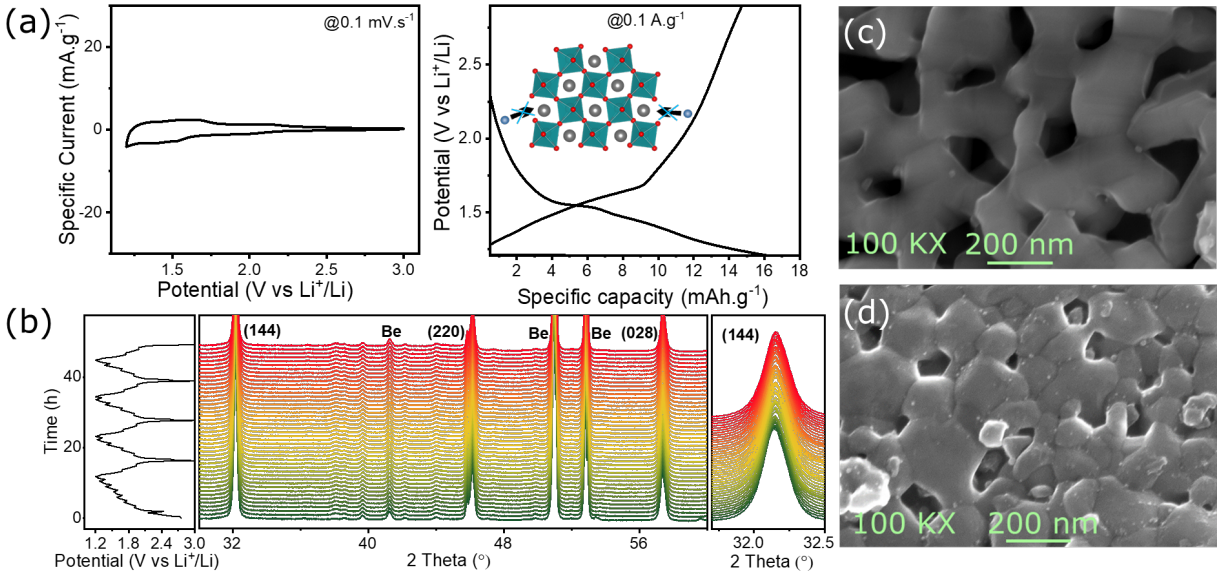

Figure 2. (a) Li^+ storage behavior of $AgNbO_3$ electrode in 1.2 – 3.0V potential window with Cyclic voltammetry and charge/discharge showing limited capacity. (b) *In-situ* XRD depicting no structural evolution and zero strain behavior upon cycling. SEM images of (c) Pristine electrode. (d) Cycled electrode showing morphology retention and surface Ag reduction (small white dots on the surface).

Ag reduction and exsolution process in $AgNbO_3$ crystal lattice

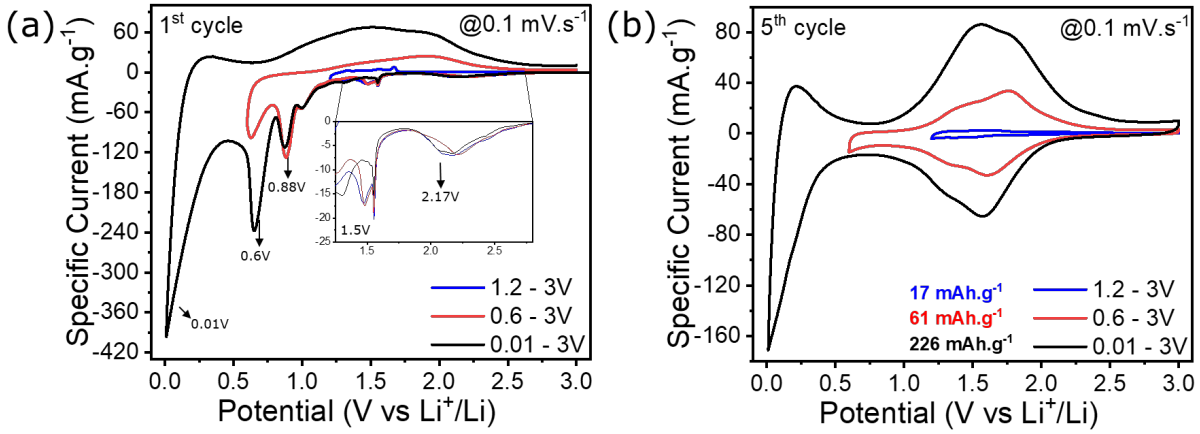

Figure 3. (a) 1st cycle of $AgNbO_3$ electrode in different potential windows using decreasing cut-off potential (1.2/0.6/0.01-3V *vs.* Li^+/Li) evidencing the activation region (0.6-0.9V) and emphasizing the appearance of irreversible activation peaks. (b) 5th cycle showing stable CV signature of the same electrodes after activation at 1.2,0.6 and 0.01V *vs.* Li^+/Li and related specific capacity values.

As mentioned in the introduction, the occurrence of *in-situ* activation as well as exsolution processes could positively contribute to the capacity of $AgNbO_3$-electrodes. Although similar process have been explored in the past for layered oxides by Morcrette [32] and Rozier *et*

al.[33], where lithium-driven displacement process allows the growth and disappearance of copper dendrites, to the best of our knowledge, the possibility to induce/promote them electrochemically in ABO_3-type structures has not yet been considered for energy storage applications. With the aim to verify this possibility, the $AgNbO_3$-based electrodes were cycled in extended potential ranges compared to the one typically used for these materials (1.2 – 3.0V *vs.* Li^+/Li), namely from 0.6 – 3.0V *vs.* Li^+/Li and from 0.01 – 3.0V *vs.* Li^+/Li.

Fig. 3a depicts the first cycles of $AgNbO_3$ in these two potential windows and, for comparison, also in the "standard" one. The tests were carried out utilizing 1M lithium bis(fluorosulfonyl)imide (LiFSI) in propylene carbonate (PC) as the electrolyte. When the potential is stopped at 1.2V *vs.* Li^+/Li, the $AgNbO_3$-based electrode displays a weak reduction peak between 2.5-2V, which is identified as the initial reduction process of surface Ag^+ in $AgNbO_3$ and can be observed in SEM imaging as clustering is starting to appear (Fig. 2d). However, it is clear that the initial reduction of silver ions is not sufficient in terms of enhancement of storage capabilities and creation of relevant sites for Li^+ insertion in $AgNbO_3$, resulting in negligible reversible capacity value (17 $mAh.g^{-1}$). This value corresponds to 15% of the A-site accessible to Li^+ cations which is consistent with a partial reduction and exsolution of Ag^+ cations thus leaving empty A sites in the $AgNbO_3$ structure at the surface of the particles.

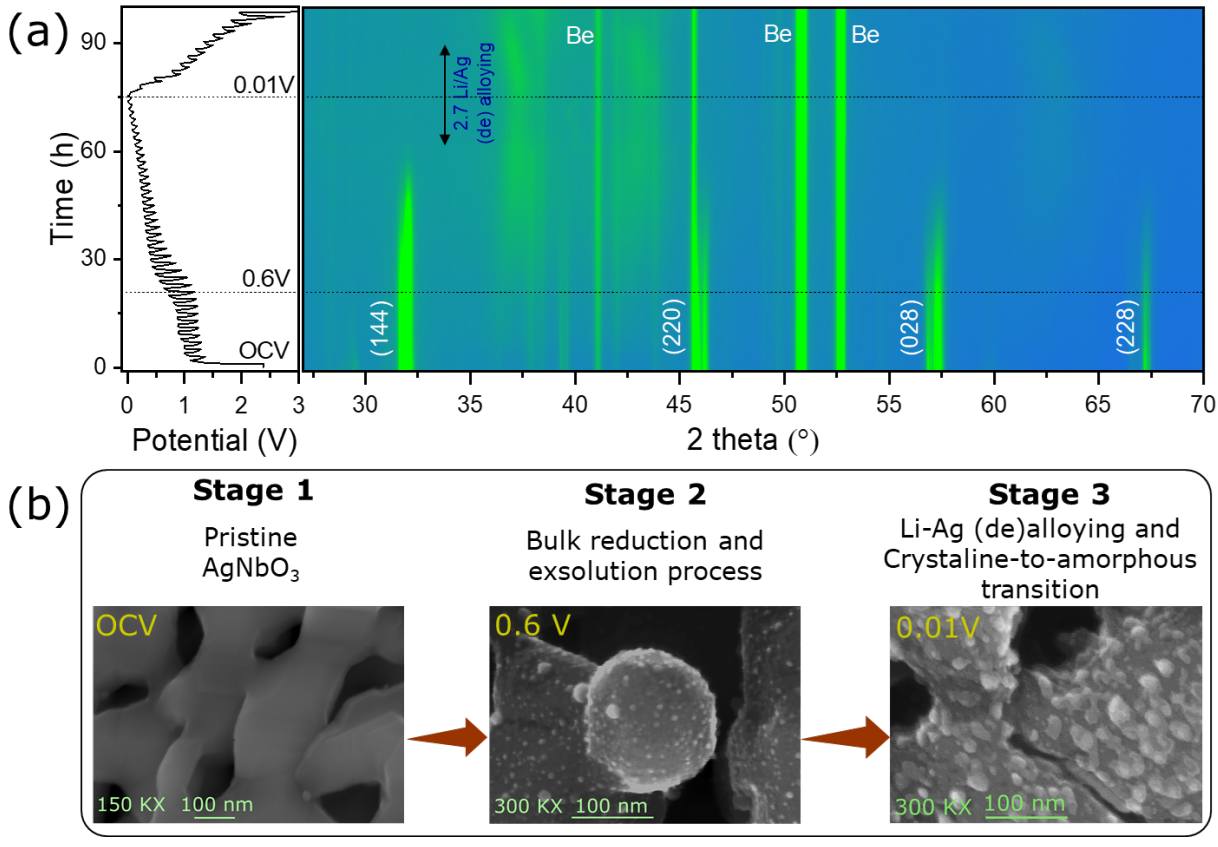

Figure 4. Li^+ storage mechanism investigation of $AgNbO_3$ electrode in 0.01 – 3.0V potential window. (a) In-situ XRD patterns of 1st charge/discharge cycles at 0.1 C. (b) Ex-situ SEM images of cycled electrode corresponding to different stages of material transition.

Lowering the electrodes cutoff potential to 0.6V *vs.* Li^+/Li resulted in the emergence of two consecutive peaks at 0.88V and 0.6V *vs.* Li^+/Li. These two peaks are also apparent when employing alternative electrolytes, some of which are known not to have SEI-forming capabilities (e.g., ionic liquid-based) (see figure S1 in SI). Therefore, it is reasonable to assume that they do not originate from interphase processes between electrode and electrolyte and/or decomposition processes on the latter, but rather come from structural processes occurring to $AgNbO_3$. Furthermore, at 0.6V *vs.* Li^+/Li, the electrochemical behavior of the electrodes changes considerably. Indeed, one can observe an enhancement of the reduction current at the same peak positions as depicted in the former 1.6-1.2V *vs.* Li^+/Li potential window (Fig. 3b), resulting in a much higher capacity (61 $mAh.g^{-1}$) (Fig. S2 & S3). *In-situ* XRD measurements, coupled with postmortem SEM and XRD (Fig. S4 & S5) indicate that the perovskite phase is preserved in the potential range between 0.6 – 3.0V *vs.* Li^+/Li. No new peaks were observed during cycling process which supports a solid solution-type mechanism occurring upon the charging process, as observed in the case of T-Nb_2O_5 [7]. Moreover, during the 1st lithiation cycle, XRD patterns above 1 V *vs.* Li^+/Li reveal the disappearance of peaks at around $2\theta = 29°$, corresponding to $Ag_2Nb_4O_{11}$ phase impurity. This suggests that a reductive potential serves as a stimulus for the impurity removal and phase purification. The mitigation of such impurities in $AgNbO_3$ perovskites has been reported previously through fine grinding process, because this impurity is typically localized within the surface layer, attributed to high-temperature melting/decomposition that initiates at the surface [34]. Furthermore, an irreversible decrease in intensity of all the crystallographic peaks is observed during 1st lithiation process (Fig. 4a) indicates that the perovskite structure is maintained at least down to 0.6V *vs.* Li^+/Li, while SEM imaging at this potential reveals an amplification of silver exsolution process at the surface of $AgNbO_3$ particles (Fig. 4b).

Alternatively, the exsolution of silver in $AgNbO_3$ can be obtained when the material is thermally reduced at 250 °C under Ar/H_2 atmosphere (Fig. S6a). However, thermal processes agglomerate silver particles into bulk-silver in comparison to the silver nanoparticles distribution obtained electrochemically (Fig. S6b). Metallic silver is detected by XRD (Fig. S6c) and concomitantly the pristine perovskite structure is still observed after thermal treatment. To summarize, decreasing the lower cut-off potential from 1.2 down to 0.6V *vs.* Li^+/Li improves the capacity of the electrode while promoting the exsolution of nanosized silver particles.

Further advantage can be taken of this peculiar microstructure by decreasing the cut-off potential down to 0.01V *vs.* Li^+/Li. Indeed, when the $AgNbO_3$-based electrodes were cycled down to 0.01V *vs.* Li^+/Li their electrochemical behavior also changed significantly. As shown in Fig. 3a, the electrodes cycled in this potential range display a capacity of 226 $mAh.g^{-1}$, which is one order of magnitude higher than that displayed by the same electrodes when a cutoff voltage at 1.2V is applied and nearly quadrupled the capacity in comparison to 0.6V cut-off (it must be said that the contribution of the conducting agent to the observed capacity is negligible, see figure S15 in SI). It is known that silver extrusion might destabilize the framework [35] and lead to structural failure and subsequent loss of capacity of the material. This is not the case for the investigated $AgNbO_3$-based electrode until the potential reaches 0.3V *vs.* Li^+/Li. Below 0.3V *vs.* Li^+/Li, and thus in the potential region considered in the test, the $AgNbO_3$ becomes amorphous with a clear loss of the diffraction peaks of the related phase (Fig. 4a). Moreover,

the formation of Li-Ag alloy take place concomitantly [36,37]. However, the reversibility of this last process for bulk Ag particles is quite poor. $AgNbO_3$-based electrodes, on the contrary, display very high reversibility and stability (Fig. S2). This latter behavior might be related to the size of the Ag particles, which are only a few nm in diameter (Fig. S6b), and might improve the reversibility of the alloying reaction due to nanosizing effect [38].

The results discussed above indicate that the perovskite structure may intrinsically stabilize Nb and generate a wide operating window for lithium-ion intercalation into the $AgNbO_3$ host structure which exhibits a lot of vacancies once silver has been exsoluted.

A summary of all these processes can be depicted from *in-situ* XRD measurements performed in the potential window between 0.01 – 3.0V *vs.* Li^+/Li (Fig. 4a). During 1st lithiation, a gradual decrease in intensity of all the crystallographic peaks occurs, till their complete disappearance, thus indicating electrochemically induced crystalline-to-amorphous transition of $AgNbO_3$. Upon delithiation, the initial peaks are not reappearing, indicating that the amorphous phase is preserved. The Ag-exsolution process causes a deviation from the ideal $AgNbO_3$ (1:1 cation) stoichiometry to A-site deficient configuration. The SEM images of cycled electrode (0.01 – 3.0V *vs.* Li^+/Li) show the growth of enlarged Ag particles on the surface compared to what is observed at 0.6 and 3.0V (Fig. 4b). It is reasonable to assume that the surface exsoluted Ag can promote the formation of diffusion channels in the structure, allowing Li^+ to freely move in as the potential decreases. The removal of Ag^+ and subsequent insertion of Li^+ cations make possible the reversible reduction of Nb^{5+} that were previously inaccessible due to the presence of silver on all the A sites of the perovskite structure.

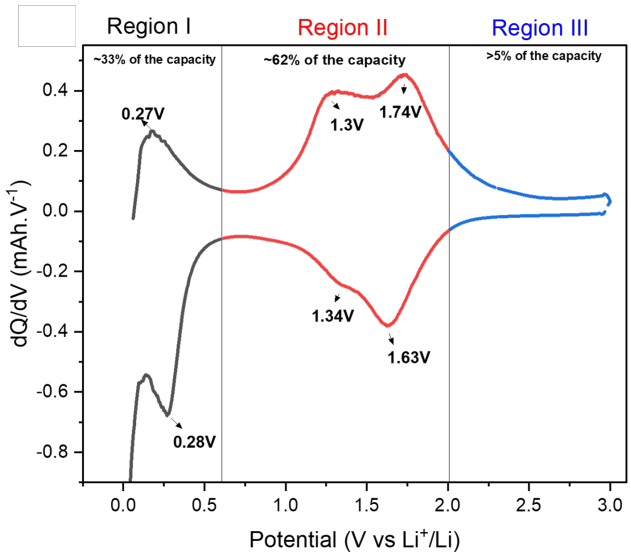

Figure 5. Differential capacity plot depicting 3 reversible redox peaks associated to region I and II respectively. Two redox peaks located at 1.74/1.63 V and 1.3/1.34 V *vs.* Li^+/Li and single peak at 0.28 V/0.27 V *vs.* Li^+/Li could be attributed to the reduction of Nb^{5+} into Nb^{3+} as well as Li-Ag alloying reaction respectively.

Further investigations of the $AgNbO_3$ electrode upon cycling were performed. Fig. 5 shows the variation of the differential capacity of $AgNbO_3$-based electrodes in the potential range between 0.01V-3V *vs.* Li^+/Li obtained from charge-discharge cycle (Fig. S7) carried out at a current

density of 0.01A.g^{-1}. It is possible to identify three distinct regions, which are contributing to the total capacity of the electrode. In the potential range between 3-2V *vs.* Li^{+}/Li (Region III) a flat signal output is observed, indicating that no significant electrochemical process is occurring and, thus, that $AgNbO_3$ is inactive in this region. However, as the potential decreases, $AgNbO_3$ starts to exhibit prominent activity with two active redox peaks at 1.74/1.63V corresponding to Nb^{5+}/Nb^{4+} [39] and 1.3/1.34V indicating reduced Nb^{4+}/Nb^{3+} [40] are observed (Region II). To back up the above assertions, it is critical to describe the oxidation state of various elements using advanced characterization tools.

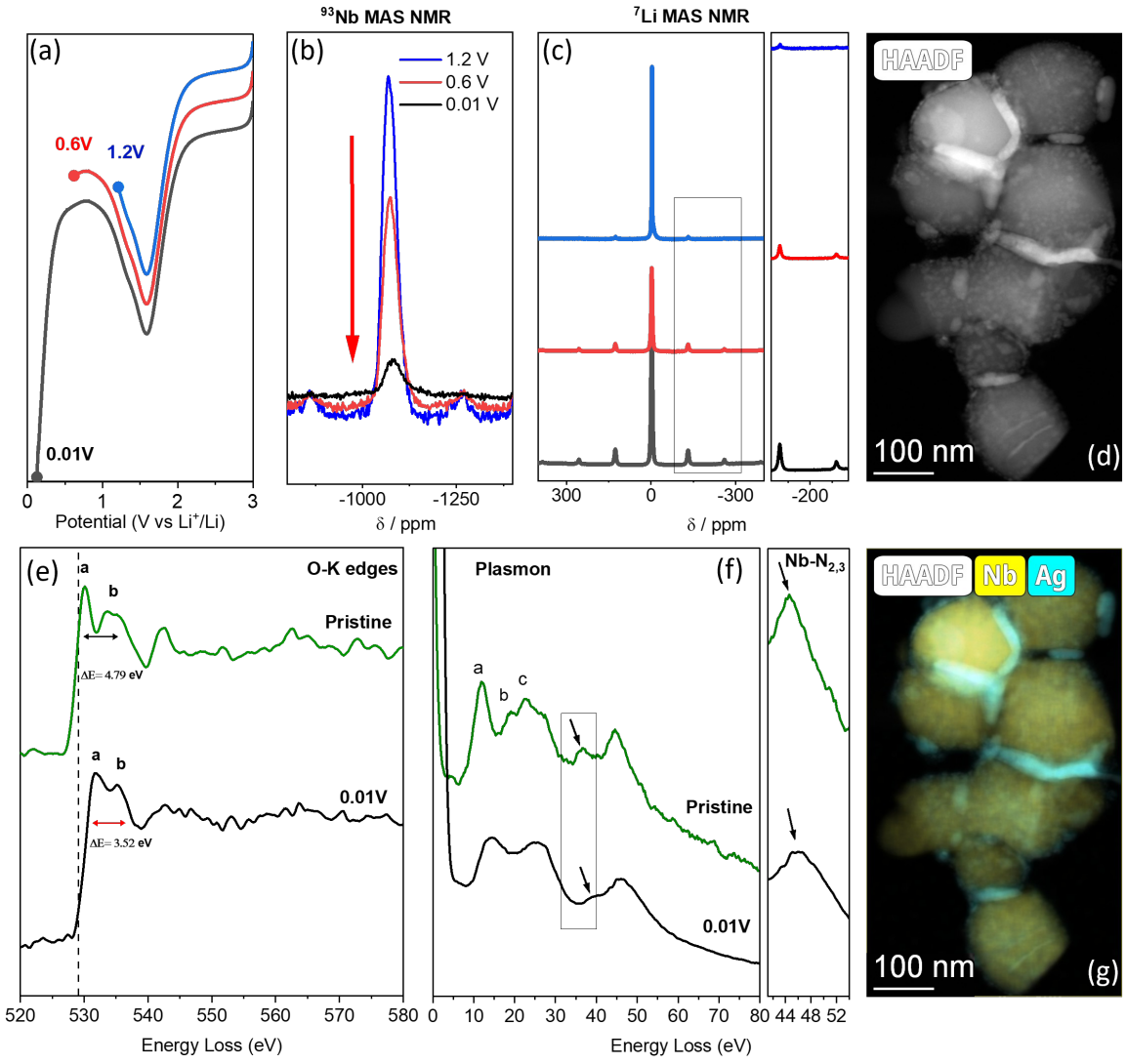

Figure 6. (a) cutoff potential for each of the associated ex-situ NMR mesurement. (b) ^{93}Niobium NMR at 1.2V (blue), 0.6V (red) and 0.01V (black) *vs.* Li^{+}/Li. (c) ^{7}Lithium NMR at 1.2,0.6 and 0.01V *vs.* Li^{+}/Li with zoom at 200 ppm. (d) and (g) HAADF-EDS mapping of $AgNbO_3$ electrode at 0.01V *vs.* Li^{+}/Li showing silver exsolution and contact between particles, as well as nanoclusters on its surface with homogeneous Niobium distribution in the particles. (e) EELS after background subtraction Fourier transformation showing the O-K edges of Pristine and Electrode at 0.01V *vs.* Li^{+}/Li. (f) plasmon region and Nb-$N_{2,3}$ edges.

Figure 6a depicts the cut-off potential for each mass normalized ^{93}Nb and ^{7}Li NMR spectra obtained from $AgNbO_3$-based electrodes during the first discharge and plotted consecutively in Figure 6b and c stopped at 1.2, 0,6 and 0.01V *vs.* Li^+/Li, respectively. Because of the diamagnetic state of Niobium (Nb^{5+}, d^0), NMR is a powerful technique for tracking niobium reduction in $AgNbO_3$, and any change in ^{93}Nb peak intensity can be correlated to the paramagnetic compounds of Nb^{3+} and Nb^{4+} (d^2 and d^1) that are not detectable by NMR, providing evidence of the change in Nb oxidation state in $AgNbO_3$-based electrodes during reduction. At 1.2V *vs.* Li^+/Li the ^{93}Nb NMR signal is clearly visible along with the corresponding sidebands which is an indication of presence of Nb^{5+} (Fig. 6b). At 0.6V, the same Nb signal is observed but the intensity is lower and suggests that some of the Nb^{5+} have been reduced along with Li^+ intercalation and thus became invisible to ^{93}Nb NMR. At 0.01V, the Nb^{5+} signal is still visible, but the signal is significantly reduced. It may indicate that the lithiation is not complete. Moreover, at 0.01V, the Nb signal appears to be broader with the beginning of a shoulder on the right side and a slight apparent shift of the maximum from -1070 to -1080 ppm. This can be an indication that the remaining Nb^{5+} are surrounded by reduced Nb^{4+} or Nb^{3+} that may provoke local distortions and modify the Nb^{5+} local environment. Fig. 6c shows ^{7}Li NMR spectra at different potentials. At 1.2V *vs.* Li^+/Li, $AgNbO_3$-based electrodes display at least three resonances. Two sharp resonances at -3.3 and 0 ppm relate to Li species most likely originating from residual electrolyte/salt in our samples; these sharp signals do not match to intercalation compounds arising from Lithium-ion. However, at 0.6 and 0.01 V *vs.* Li^+/Li, there is a noticeable increase in a ^{7}Li NMR resonance signal which is consistent with the presence of Li^+ providing us an indication of intercalation into the active material.

Further investigations were then carried out using electron energy loss spectroscopy (EELS). Figure 6e shows O-K edges for $AgNbO_3$-based electrodes in pristine (Nb^{+5}) and electrodes cycled at 0.01V *vs.* Li^+/Li to highlight the potential difference in niobium oxidation state. First, O-K edge is characterized by a typical double-peak feature near the peak onset, which is characteristic of transition metal oxides [41]. This suggests that the investigated sample is not reduced to Nb^0, in agreement with the NMR results. Furthermore, in comparison to pristine $AgNbO_3$-based electrodes, a shift in peak onset as well as a peak intensity reduction between peak a and b, associated with the O-K edge of Nb at 0.01V *vs.* Li^+/Li, was observed. The energy difference ΔE between these two peaks was also reduced from 4.79eV for the pristine sample (Nb^{5+}) to 3.52eV in the electrode cycled at 0.01V *vs.* Li^+/Li. This behavior is comparable to that observed by Bach *et al*. and Tao *et al.* for niobium oxides and derivatives [42,43]. Furthermore, Nb-$N_{2,3}$ edges that appear in the low-loss region can be attributed to transitions of Nb 4p electrons to unoccupied 4d and 5s. This lead to a peak broadening with the appearance of a shoulder at around 44eV (Fig. 6f), which was also previously correlated to a decrease of Nb valence in niobium oxides [42,44]. These results indicate the occurrence of a shift in the oxidation state of Nb towards lower valence states. However, to determine the exact degree of oxidation is difficult. Nonetheless, the ΔE energy difference on the O-K edges in reduced $AgNbO_3$ electrode (ΔE=3.52eV) can be linearly associated with valence states of niobium oxides [42], suggesting an averaged out +3.66 oxidation state for Nb in the $AgNbO_3$-based electrode at 0.01V *vs.* Li^+/Li ($Nb^{+3.66}$) (Fig. S8) which is in agreement with the electrochemical results.

Finally, below 0.6V *vs.* Li^+/Li, a new reaction seems to take place. It leads to approximately 70 $mAh.g^{-1}$, which accounts for 2.72 lithium per silver atom, as depicted from Figure 5. According to previous studies on Li-Ag alloying [45] as well as to the Li-Ag binary diagram (Fig. S9), one can suspect that Ag-Li alloying reactions are taking place at such low potential region. In the lithium-silver binary diagram, 2.72 lithium per silver atom corresponds to the γ_3 phase with redox peaks at 0.28/0.27 V *vs.* Li^+/Li associated to Li-Ag alloying [36,46]. An indirect approach is adopted to confirm these results, where Ag-nanoparticles electrode were cycled vs. metallic Li keeping the same experimental conditions. The findings reveal a Li/Ag ratio of 2.61 in the alloying process, indicating that the system falls between the γ_3 and γ_2 phases (Fig. S9 & S10) in agreement with Ag-Li alloying obtained in $AgNbO_3$. Finally, HAADF-EDS imaging of $AgNbO_3$-based electrodes at 0.01V *vs.* Li^+/Li were carried out. As shown in Fig. 6d and g, the occurrence of silver extrusion in the cycled electrode compared to the pristine one (Fig. S11 and S12), takes place without affecting Niobium concentration in the material (Fig. 6g). Silver can be seen to percolate particles and grain boundaries but also cluster as nanoparticles at the surface (Fig. 6d and g), which could potentially play a substantial role in increasing the power capability of $AgNbO_3$-based electrodes by improving the electronic conductivity between the grains and further contributes to improved reversibility of electrochemical Ag-Li alloying reaction.

Moreover, According to [36,45,46] and [47,48], the theoretical capacity of $AgNbO_3$ (including a full reduction of Ag^+ to Ag^0 and Nb^{5+} to Nb^{3+}, and the formation of $Li_{2.72}Ag$ alloy) should reach 604 $mAh.g^{-1}$. The maximum capacity obtained upon the first reduction is 450 $mAh.g^{-1}$, thus suggesting only a partial reduction of Nb^{5+} to Nb^{3+}, and some Ag^0 particles not involved in alloying reaction with lithium. It can be noted that the maximum capacity for 12 wt% $Ag_2Nb_4O_{11}$ impurity leads to a contribution to the overall capacity of max. 24 mAh/g, i.e. 5% of the $AgNbO_3$ maximum capacity.

Considering the results discussed above, it appears that the $AgNbO_3$-based electrodes undergo a transition from pristine state (Fig. 7a, stage 1) to Ag-exsolution from A-site of the lattice (Stage 2), and finally to a crystalline-to-amorphous transition and concomitant Li-Ag alloying reaction (stage 3). Fig. 7b and c indicate what occurs to the $AgNbO_3$ electrode from a structural and electrochemical point of view. Undoubtfully, the silver exsolution process accounts for a major part to the reversibility of further reversible reactions.

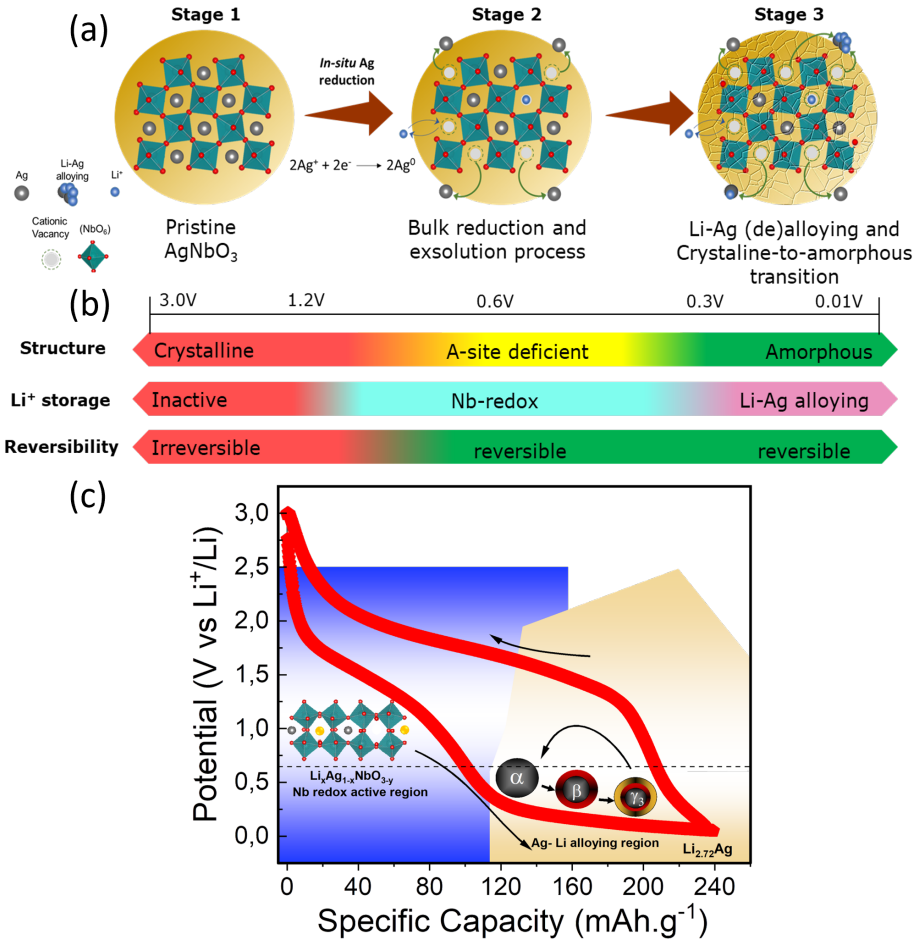

Figure 7. (a) Schematic representation of whole in-situ material transformation due to surface and bulk Ag reduction, exsolution of Ag nanoparticles, crystalline-to-amorphous transformation, and nanoscale Ag-Li alloying process. (b) Overall summary of material transition and Li^+ storage mechanisms involved in $AgNbO_3$ material. (c) $AgNbO_3$ specific capacity and its associated schematic redox activity and phase changes according to Li-Ag binary phase diagram at room temperature. As the potential decreases, Li-Ag alloying undergoes several phases transitions until γ_3 phase.

2.1 Electrochemical performance characterization

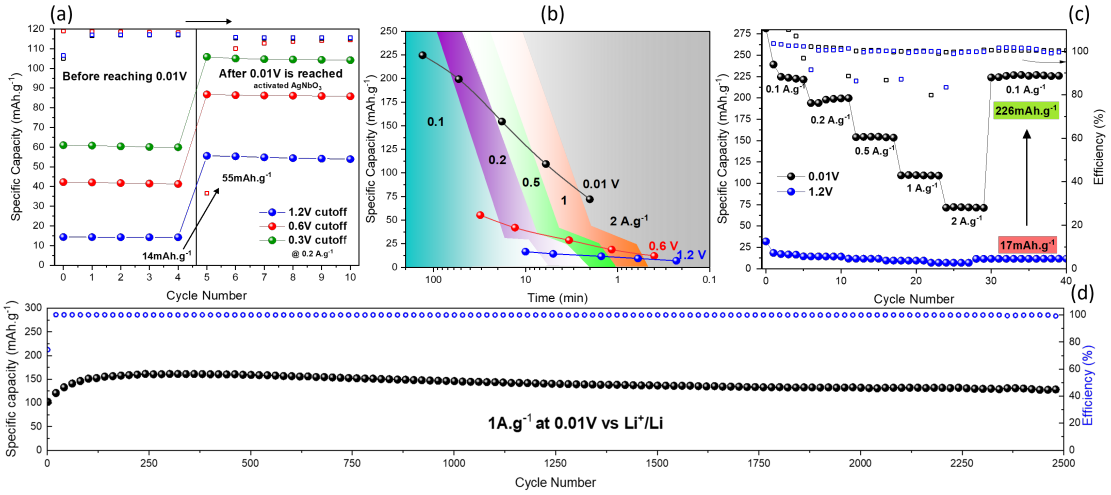

Figure 8 (a) specific capacity of $AgNbO_3$ electrode before activation (left) and after activation (right) at 0.2 $A.g^{-1}$. (b) Specific capacity versus discharge time for $AgNbO_3$ electrode at 1.2, 0.6, and 0.3 V *vs.* Li^+/Li. (c) rate test of $AgNbO_3$ at 0.01V (black) and 1.2V (blue) *vs.* Li^+/Li. The capacity has been multiplied by 13 for the same electrode at the same current density. (d) Stability test at 1 $A.g^{-1}$ charge/discharge for 2500 cycles. These plots have been recorded after the initial cycles reported in Fig. 3.

To understand the impact of the structural changes discussed above, the electrochemical performances of the $AgNbO_3$-based electrodes were investigated at various cutoff potentials. Fig. 8a shows the specific capacity of $AgNbO_3$-based electrode before and after activation with galvanostatic cycling at 1.2, 0.6, and 0.3 V *vs.* Li^+/Li, respectively. As shown, $AgNbO_3$-based electrodes achieve activation which allows a significant and permanent increase of their capacity. *e.g.*, from 14 $mAh.g^{-1}$ at 0.3 V before activation to 55 $mAh.g^{-1}$ at 0.3 V after activation. This activation behavior is seen to improve capacity continuously as the potential decreases up to 0.01V *vs.* Li^+/Li, in agreement with previous discussions regarding vacancies for lithium intercalation once silver has been exsoluted from the structure. To better understand the effect of activation on the power performance and diffusion kinetics of $AgNbO_3$, time-rate dependency was studied, where different current densities were applied at different cutoff potentials (Fig. 8b). From this study, it is obvious that the activation process is significantly enhancing the energy density of the $AgNbO_3$-based electrodes. Furthermore, discharge cycles can be carried out in less than 2 minutes while maintaining a capacity of 72 $mAh.g^{-1}$.

The lithium diffusion coefficient calculated for the activated $AgNbO_3$ electrode from GITT measurements (Fig. S13) is in the order ~10^{-11}-10^{-12} $cm^2\ s^{-1}$, which is a value comparable to the reported high-rate intercalation type anode materials [49,50]. Another important parameter to consider when studying high-rate anode materials is their stability under severe current load conditions. Fig. 8c depicts rate performance of $AgNbO_3$-based electrodes at 0.01V and 1.2V *vs.* Li^+/Li. As shown, the activated $AgNbO_3$-based electrodes display remarkable efficiency and fair rate performance, with capacities reaching 226 $mAh.g^{-1}$, 200 $mAh.g^{-1}$, 155 $mAh.g^{-1}$, 110

mAh.g^{-1} and 72 mAh.g^{-1} at 0.1 A.g^{-1}, 0.2 A.g^{-1}, 0.5 A.g^{-1}, 1 A.g^{-1}, and 2 A.g^{-1}, respectively. Moreover, when the current density is reduced again to 0.1 A.g^{-1}, the initial capacity is fully recovered, demonstrating the high reversibility and stability of the system to various current densities.

Finally, cycling stability of the $AgNbO_3$-based electrodes has been investigated carrying out charge-discharge cycles at 1A.g^{-1}. As shown in Fig. 8d, $AgNbO_3$-based electrodes display very high cycling efficiency (higher than 99,9%) as they go through activation, and they retain all their initial capacity after 2500 cycles. The good performance of the electrode is also maintained when is used in a proof-of-concept lab scale LIB cell (see figure S14). These results indicate that the investigated electrodes are a promising model electrode for high-power applications and pave the way for novel *exsoluted* and stable ABO_3-type electrodes for high-power lithium storage.

4. Conclusion

This work reported the preparation and investigation of perovskite type $AgNbO_3$ as a model material for negative electrode in LIBs. During 1st lithiation, a unique activation process is observed due to Ag-exsolution from A-site of structure causing A/B non-stoichiometry, which results in a compensation of Ag^+ by Li^+ cation intercalation to a certain extent. Structural transition between crystalline to amorphous oxide is observed below 0.3V *vs.* Li^+/Li. Lithium insertion is accompanied by Nb^{5+} reduction down to an average value of $Nb^{+3.66}$. Moreover, we have demonstrated the reversible Li-Ag nano (de)alloying charge storage mechanisms in this perovskite material at the end of the reduction process. Overall, $AgNbO_3$ delivered a specific capacity of 226 mAh.g^{-1} in extended potential window (0.01 – 3.0V), which is thirteen-fold compared to the capacity of material in its electrochemically stable potential window (1.2 – 3.V) and 4 folds capacity in comparison to the Nb-electrochemically active (0.6-3V) region. Furthermore, the outstanding capabilities of such electrode in high-power conditions with a capacity retention of 72 mAh.g^{-1} at 2A.g^{-1} and a very good cycling stability and efficiency at 1A.g^{-1} after 2500 cycles were demonstrated. This work opens the way for exploring the fascinating properties of exsolved ABO_3 type perovskites and provides a foundation for their utilization as design material for high power Lithium-ion intercalating perovskite anodes.

Acknowledgments

The authors wish to thank the Université de Nantes and Friedrich-Schiller University Jena for their financial support. Abbas Khan and Metin Orbay, as a part of the DESTINY PhD programme (Doctorate programme on Emerging battery Storage Technologies INspiring Young scientists) acknowledge funding from the European Union's Horizon 2020 research and innovation programme under the Marie Skłodowska-Curie Actions Cofund Grant Agreement No: 945357. Measurements which were performed on IMN's equipment(s) platform, PLASSMAT, Nantes, France. Funded by the French Contrat Plan Etat-Région and the European Regional Development Fund of Pays de la Loire, the CIMEN Electron Microscopy

Center in Nantes, France, is greatly acknowledged. The authors are deeply thankful to Dr. Eric Quarez (from Institut des Matériaux de Nantes Jean Rouxel, IMN) for performing Rietveld refinements presented in this research paper.

References

[1] M. Armand, J.-M. Tarascon, Building better batteries, Nature 451 (2008) 652–657. https://doi.org/10.1038/451652a.
[2] B. Babu, P. Simon, A. Balducci, Fast Charging Materials for High Power Applications, Advanced Energy Materials 10 (2020) 2001128. https://doi.org/10.1002/aenm.202001128.
[3] M. Schroeder, S. Menne, J. Ségalini, D. Saurel, M. Casas-Cabanas, S. Passerini, M. Winter, A. Balducci, Considerations about the influence of the structural and electrochemical properties of carbonaceous materials on the behavior of lithium-ion capacitors, Journal of Power Sources 266 (2014) 250–258. https://doi.org/10.1016/j.jpowsour.2014.05.024.
[4] T.-F. Yi, S.-Y. Yang, Y. Xie, Recent advances of Li4Ti5O12 as a promising next generation anode material for high power lithium-ion batteries, J. Mater. Chem. A 3 (2015) 5750–5777. https://doi.org/10.1039/C4TA06882C.
[5] T. Wang, T. Ge, S. Shi, M. Wu, G. Yang, Synthesis of wolframite FeNbO4 nanorods as a novel anode material for improved lithium storage capability, Journal of Alloys and Compounds 740 (2018) 7–15. https://doi.org/10.1016/j.jallcom.2017.12.369.
[6] T. Takashima, T. Tojo, R. Inada, Y. Sakurai, Characterization of mixed titanium–niobium oxide Ti2Nb10O29 annealed in vacuum as anode material for lithium-ion battery, Journal of Power Sources 276 (2015) 113–119. https://doi.org/10.1016/j.jpowsour.2014.11.109.
[7] J. Come, V. Augustyn, J.W. Kim, P. Rozier, P.-L. Taberna, P. Gogotsi, J.W. Long, B. Dunn, P. Simon, Electrochemical Kinetics of Nanostructured Nb2O5 Electrodes, J. Electrochem. Soc. 161 (2014) A718. https://doi.org/10.1149/2.040405jes.
[8] K.J. Griffith, Y. Harada, S. Egusa, R.M. Ribas, R.S. Monteiro, R.B. Von Dreele, A.K. Cheetham, R.J. Cava, C.P. Grey, J.B. Goodenough, Titanium Niobium Oxide: From Discovery to Application in Fast-Charging Lithium-Ion Batteries, Chem. Mater. 33 (2021) 4–18. https://doi.org/10.1021/acs.chemmater.0c02955.
[9] G.A. Samara, The relaxational properties of compositionally disordered ABO3 perovskites, J. Phys.: Condens. Matter 15 (2003) R367. https://doi.org/10.1088/0953-8984/15/9/202.
[10] N. Ramadass, ABO3-type oxides—Their structure and properties—A bird's eye view, Materials Science and Engineering 36 (1978) 231–239. https://doi.org/10.1016/0025-5416(78)90076-9.
[11] L. Zhang, X. Zhang, G. Tian, Q. Zhang, M. Knapp, H. Ehrenberg, G. Chen, Z. Shen, G. Yang, L. Gu, F. Du, Lithium lanthanum titanate perovskite as an anode for lithium ion batteries, Nat Commun 11 (2020) 3490. https://doi.org/10.1038/s41467-020-17233-1.
[12] A. Chaupatnaik, P. Barpanda, Perovskite lead-based oxide anodes for rechargeable batteries, Electrochemistry Communications 127 (2021) 107038. https://doi.org/10.1016/j.elecom.2021.107038.
[13] E. Le Calvez, J.C. Espinosa-Angeles, G.J. Whang, N. Dupré, B.S. Dunn, O. Crosnier, T. Brousse, Investigating the Perovskite Ag1-3xLaxNbO3 as a High-Rate Negative Electrode for Li-Ion Batteries, Front. Chem. 10 (2022) 873783. https://doi.org/orb.
[14] J.W. Kim, V. Augustyn, B. Dunn, The Effect of Crystallinity on the Rapid Pseudocapacitive Response of Nb2O5, Advanced Energy Materials 2 (2012) 141–148. https://doi.org/10.1002/aenm.201100494.
[15] L. Yang, X. Xiong, G. Liang, X. Li, C. Wang, W. You, X. Zhao, X. Liu, R. Che, Atomic Short-Range Order in a Cation-Deficient Perovskite Anode for Fast-Charging and Long-Life Lithium-Ion Batteries, Advanced Materials 34 (2022) 2200914. https://doi.org/10.1002/adma.202200914.
[16] Y. Zhou, E. Le Calvez, S.W. Baek, M. Frajnkovič, C. Douard, E. Gautron, O. Crosnier, T. Brousse, L. Pilon, Effect of particle size on thermodynamics and lithium ion transport in electrodes made of Ti2Nb2O9 microparticles or nanoparticles, Energy Storage Materials 52 (2022) 371–385. https://doi.org/10.1016/j.ensm.2022.08.010.
[17] V. Aravindan, J. Sundaramurthy, A. Jain, P.S. Kumar, W.C. Ling, S. Ramakrishna, M.P. Srinivasan, S. Madhavi, Unveiling TiNb2O7 as an Insertion Anode for Lithium Ion Capacitors with High Energy and Power Density, ChemSusChem 7 (2014) 1858–1863. https://doi.org/10.1002/cssc.201400157.
[18] E.L. Calvez, N. Dupré, É. Gautron, C. Douard, O. Crosnier, T. Brousse, Effect of particle microstructure and the role of proton on the lithium insertion properties of HTiNbO5 electrode material, Electrochimica Acta 455 (2023) 142432. https://doi.org/10.1016/j.electacta.2023.142432.

[19] X. Li, Z. Lin, N. Jin, L. Sun, X. Yang, Y. Liu, High-capacity anode materials for lithium-ion batteries: perovskite strontium vanadate with crystalline-amorphous dual-phase structure, Materials Today Chemistry 30 (2023) 101542. https://doi.org/10.1016/j.mtchem.2023.101542.
[20] X. Li, Z. Lin, N. Jin, L. Sun, X. Yang, Y. Liu, Electrochemically Induced Crystalline-to-Amorphous Transition of Dinuclear Polyoxovanadate for High-Rate Lithium-Ion Batteries, Advanced Functional Materials 33 (2023) 2214667. https://doi.org/10.1002/adfm.202214667.
[21] D. Neagu, V. Kyriakou, I.-L. Roiban, M. Aouine, C. Tang, A. Caravaca, K. Kousi, I. Schreur-Piet, I.S. Metcalfe, P. Vernoux, M.C.M. van de Sanden, M.N. Tsampas, In Situ Observation of Nanoparticle Exsolution from Perovskite Oxides: From Atomic Scale Mechanistic Insight to Nanostructure Tailoring, ACS Nano 13 (2019) 12996–13005. https://doi.org/10.1021/acsnano.9b05652.
[22] K. Kousi, C. Tang, I.S. Metcalfe, D. Neagu, Emergence and Future of Exsolved Materials, Small 17 (2021) 2006479. https://doi.org/10.1002/smll.202006479.
[23] H. Jeong, Y.H. Kim, B.-R. Won, H. Jeon, C. Park, J. Myung, Emerging Exsolution Materials for Diverse Energy Applications: Design, Mechanism, and Future Prospects, Chem. Mater. 35 (2023) 3745–3764. https://doi.org/10.1021/acs.chemmater.3c00004.
[24] J.H. Kim, J.K. Kim, J. Liu, A. Curcio, J.-S. Jang, I.-D. Kim, F. Ciucci, W. Jung, Nanoparticle Ex-solution for Supported Catalysts: Materials Design, Mechanism and Future Perspectives, ACS Nano 15 (2021) 81–110. https://doi.org/10.1021/acsnano.0c07105.
[25] S. Wang, D. Li, C. Yang, G. Sun, J. Zhang, Y. Xia, C. Xie, G. Yang, M. Zhou, W. Liu, A novel method for the synthesize of nanostructured MgFe2O4 photocatalysts, J Sol-Gel Sci Technol 84 (2017) 169–179. https://doi.org/10.1007/s10971-017-4471-3.
[26] J.B. Leriche, S. Hamelet, J. Shu, M. Morcrette, C. Masquelier, G. Ouvrard, M. Zerrouki, P. Soudan, S. Belin, E. Elkaïm, F. Baudelet, An Electrochemical Cell for Operando Study of Lithium Batteries Using Synchrotron Radiation, J. Electrochem. Soc. 157 (2010) A606. https://doi.org/10.1149/1.3355977.
[27] C. Leibing, A. Balducci, Glyoxylic-Acetal-Based Electrolytes in Combination with Soft and Hard Carbon Electrodes for Lithium-Ion Batteries: An Evaluation of Room and High Temperature Performance, J. Electrochem. Soc. 168 (2021) 090533. https://doi.org/10.1149/1945-7111/ac23a2.
[28] P. Sciau, A. Kania, B. Dkhil, E. Suard, A. Ratuszna, Structural investigation of AgNbO3 phases using x-ray and neutron diffraction, J. Phys.: Condens. Matter 16 (2004) 2795. https://doi.org/10.1088/0953-8984/16/16/004.
[29] Y. Tian, P. Song, G. Viola, J. Shi, J. Li, L. Jin, Q. Hu, Y. Xu, W. Ge, Z. Yan, D. Zhang, N.V. Tarakina, I. Abrahams, X. Wei, H. Yan, Silver niobate perovskites: structure, properties and multifunctional applications, J. Mater. Chem. A 10 (2022) 14747–14787. https://doi.org/10.1039/D2TA00905F.
[30] S.F. Wang, H.B. Lv, X.S. Zhou, Y.Q. Fu, X.T. Zu, Magnetic Nanocomposites Through Polyacrylamide Gel Route, Nanoscience and Nanotechnology Letters 6 (2014) 758–771. https://doi.org/10.1166/nnl.2014.1796.
[31] Y. Yang, J. Zhao, Wadsley–Roth Crystallographic Shear Structure Niobium-Based Oxides: Promising Anode Materials for High-Safety Lithium-Ion Batteries, Advanced Science 8 (2021) 2004855. https://doi.org/10.1002/advs.202004855.
[32] M. Morcrette, P. Rozier, L. Dupont, E. Mugnier, L. Sannier, J. Galy, J.-M. Tarascon, A reversible copper extrusion–insertion electrode for rechargeable Li batteries, Nature Mater 2 (2003) 755–761. https://doi.org/10.1038/nmat1002.
[33] P. Rozier, M. Morcrette, O. Szajwaj, V. Bodenez, M. Dolle, C. Surcin, L. Dupont, J.M. Tarascon, Li-Driven Copper Extrusion/Re-injection in Various Cu-based Oxides and Sulfides, Israel Journal of Chemistry 48 (2008) 235–249. https://doi.org/10.1560/IJC.48.3-4.249.
[34] Y. Tian, P. Song, G. Viola, J. Shi, J. Li, L. Jin, Q. Hu, Y. Xu, W. Ge, Z. Yan, D. Zhang, N.V. Tarakina, I. Abrahams, X. Wei, H. Yan, Silver niobate perovskites: structure, properties and multifunctional applications, J. Mater. Chem. A 10 (2022) 14747–14787. https://doi.org/10.1039/D2TA00905F.
[35] J.H. Kim, J.K. Kim, J. Liu, A. Curcio, J.-S. Jang, I.-D. Kim, F. Ciucci, W. Jung, Nanoparticle Ex-solution for Supported Catalysts: Materials Design, Mechanism and Future Perspectives, ACS Nano 15 (2021) 81–110. https://doi.org/10.1021/acsnano.0c07105.
[36] J.S. Corsi, A.K. Ng, Y. Huang, E. Detsi, Impact of the Gibbs–Thomson Effect on Lithium Solubility in Silver Used as an Alloy Lithium-Ion Battery Anode, ACS Appl. Energy Mater. 5 (2022) 4547–4555. https://doi.org/10.1021/acsaem.1c04127.
[37] S. Jin, Y. Ye, Y. Niu, Y. Xu, H. Jin, J. Wang, Z. Sun, A. Cao, X. Wu, Y. Luo, H. Ji, L.-J. Wan, Solid–Solution-Based Metal Alloy Phase for Highly Reversible Lithium Metal Anode, J. Am. Chem. Soc. 142 (2020) 8818–8826. https://doi.org/10.1021/jacs.0c01811.
[38] X. Li, G. Yang, S. Zhang, Z. Wang, L. Chen, Improved lithium deposition on silver plated carbon fiber paper, Nano Energy 66 (2019) 104144. https://doi.org/10.1016/j.nanoen.2019.104144.

[39] C. Yang, S. Yu, C. Lin, F. Lv, S. Wu, Y. Yang, W. Wang, Z.-Z. Zhu, J. Li, N. Wang, S. Guo, Cr0.5Nb24.5O62 Nanowires with High Electronic Conductivity for High-Rate and Long-Life Lithium-Ion Storage, ACS Nano 11 (2017) 4217–4224. https://doi.org/10.1021/acsnano.7b01163.
[40] M. Yang, S. Li, J. Huang, Three-Dimensional Cross-Linked Nb2O5 Polymorphs Derived from Cellulose Substances: Insights into the Mechanisms of Lithium Storage, ACS Appl. Mater. Interfaces 13 (2021) 39501–39512. https://doi.org/10.1021/acsami.1c11720.
[41] F.M.F. de Groot, M. Grioni, J.C. Fuggle, J. Ghijsen, G.A. Sawatzky, H. Petersen, Oxygen 1s x-ray-absorption edges of transition-metal oxides, Phys. Rev. B 40 (1989) 5715–5723. https://doi.org/10.1103/PhysRevB.40.5715.
[42] D. Bach, R. Schneider, D. Gerthsen, J. Verbeeck, W. Sigle, EELS of Niobium and Stoichiometric Niobium-Oxide Phases—Part I: Plasmon and Near-Edges Fine Structure, Microscopy and Microanalysis 15 (2009) 505–523. https://doi.org/10.1017/S143192760999105X.
[43] R. Tao, R. Todorovic, J. Liu, R.J. Meyer, A. Arnold, W. Walkosz, P. Zapol, A. Romanenko, L.D. Cooley, R.F. Klie, Electron energy-loss spectroscopy study of metallic Nb and Nb oxides, Journal of Applied Physics 110 (2011) 124313. https://doi.org/10.1063/1.3665193.
[44] D. Bach, R. Schneider, D. Gerthsen, EELS of Niobium and Stoichiometric Niobium-Oxide Phases—Part II: Quantification, Microscopy and Microanalysis 15 (2009) 524–538. https://doi.org/10.1017/S1431927609991061.
[45] C.-M. Park, H. Jung, H.-J. Sohn, Electrochemical Behaviors and Reaction Mechanism of Nanosilver with Lithium, Electrochem. Solid-State Lett. 12 (2009) A171. https://doi.org/10.1149/1.3152570.
[46] H. Okamoto, Supplemental Literature Review of Binary Phase Diagrams: Ag-Li, Ag-Sn, Be-Pu, C-Mn, C-Si, Ca-Li, Cd-Pu, Cr-Ti, Cr-V, Cu-Li, La-Sc, and Li-Sc, J. Phase Equilib. Diffus. 38 (2017) 70–81. https://doi.org/10.1007/s11669-016-0504-9.
[47] T. Brousse, D. Defives, L. Pasquereau, S.M. Lee, U. Herterich, D.M. Schleich, Metal oxide anodes for Li-ion batteries, Ionics 3 (1997) 332–337. https://doi.org/10.1007/BF02375707.
[48] G. Taillades, J. Sarradin, Silver: high performance anode for thin film lithium ion batteries, Journal of Power Sources 125 (2004) 199–205. https://doi.org/10.1016/j.jpowsour.2003.07.004.
[49] K.J. Griffith, K.M. Wiaderek, G. Cibin, L.E. Marbella, C.P. Grey, Niobium tungsten oxides for high-rate lithium-ion energy storage, Nature 559 (2018) 556–563. https://doi.org/10.1038/s41586-018-0347-0.
[50] X. Li, Z. Lin, N. Jin, X. Yang, Y. Du, L. Lei, P. Rozier, P. Simon, Y. Liu, Perovskite-Type SrVO3 as High-Performance Anode Materials for Lithium-Ion Batteries, Advanced Materials 34 (2022) 2107262. https://doi.org/10.1002/adma.202107262.

Graphical Abstract